ORIGINAL PAPER

Preparation, characterization and evaluation of a novel CMC/Chitosan-α-Fe$_2$O$_3$ nanoparticles-coated 17–4 PH stainless-steel foam

Selcan Karakuş[1] · İnci Albayrak[2] · Nuray Beköz Üllen[3] · Mert Akin Insel[4] · Ayben Kilislioğlu[5]

Abstract

In this study, we fabricated a novel CMC/Chitosan-α-Fe$_2$O$_3$ nanoparticles (NPs)-coated 17–4 PH stainless-steel foam. The CMC/Chitosan matrix was preferred as a stabilizing role in the uniform dispersion of α-Fe$_2$O$_3$ NPs in the colloidal solution. The BET, SEM/EDX, XRD, and FT-IR techniques were used to determine the functional groups and surface of the nanostructure. The α-Fe$_2$O$_3$ NPs were uniformly dispersed and had a spherical shape with an average particle size of 10–20 nm with a surface area of 180.37 m^2/g. Additionally, we examined to identify the physicochemical properties of the α-Fe$_2$O$_3$ NPs under ultrasonic irradiation. According to SEM results, we found that the average particle size of CMC/Chitosan-α-Fe$_2$O$_3$ NPs was between 10 and 20 nm with a spherical shape. We observed the effects of the operating parameters such as the concentration (0–1 ppm), mass fraction (10–20%) of silica, mass fraction (1–5%) of CTAB, temperature (25–45 °C), pH (3–10), sonication time (5–20 min), and the amplitude of sonication (10–40%). A mathematical modeling was performed, which related surface tension via the operating variables. The critical micelle concentrations were found 0.399, 0.428, and 0.573 ppm for mass fractions 10, 15, and 20% of silica, respectively. An error analysis was conducted in order to evaluate the physicochemical properties of the constructed models. Results showed that the effect of ultrasonic irradiation on the surface tension of biopolymer blend based α-Fe$_2$O$_3$ NPs and the design of uniform stainless-steel foam with α-Fe$_2$O$_3$ NPs coatings.

Keywords A-Fe$_2$O$_3$ nanoparticles · Surface tension · Chitosan · Biopolymer

✉ Nuray Beköz Üllen
  nbekoz@istanbul.edu.tr

Extended author information available on the last page of the article

⚫ Springer

Introduction

Iron oxide nanoparticles have been commonly preferred due to their unique bio-compatibility, tunable surface modifications, magnetic, chemical, biological, and electrical properties in various fields of industrial applications and approved by the US Food and Drug Administration (FDA) for use on the clinical studies [1–5]. Surface modification with nanomaterials such as iron oxide nanoparticles provide an advantage in the field of drug delivery, magnetic resonance imaging (MRI), and theragnostic for biomedical applications [6].

Recently, the various studies have reported on the NPs have received attention due to their large surface area, excellent catalytic activity and morphological features (shape, size and dimension, surface activity, and low reduction potential [7–12]. Especially, the preparation of iron oxide NPs was reported using different methods such as chemical precipitation [13], sol–gel [14], ultrasonic irradiation [15], and emulsion methods [16] in previous studies. In this study, we prepared the CMC/Chitosan-α-Fe$_2$O$_3$ NPs using the green and low-cost ultrasonic irradiation method and we coated onto the surface of 17–4 PH stainless-steel foam with polymer blend-α-Fe$_2$O$_3$ NPs to fabricate the novel bio-nanomaterial. We noticed that no studies had reported in the literature regarding the coating of 17–4 PH stainless-steel foam with polymer blend-α-Fe$_2$O$_3$ NPs. Therefore, we focused on this surface modification of 17–4 PH stainless-steel foam in this study.

17–4 PH stainless-steel foam is suitable for use as a biomaterial due to its excellent mechanical and biological properties such as easy producibility, high porosity, corrosion resistance, strength, and biocompatibility [17–19]. Surface modification of the stainless-steel foams depends on some critical factors such the homogeneous distribution, particle morphology, sinter density, and sensitization [20]. Based on our previous experience, we used synthesized CMC/Chitosan-α-Fe$_2$O$_3$ NPs due to their characteristic properties such as their nanoscale size, shape, high surface area, chemical property, and surface chemistry and we investigated the effect of surface modification on the surface characteristics and surface chemistry of the structure [21]. We evaluated the change in surface tension with different sonication inputs such as time, power, and amplitude on nanosystem formation and stabilization based on the surface tension behaviors. Furthermore, we defined the correlation between surface tension and surface modification, which depends on the types of sonication inputs and experimental parameters. This correlation was examined with the characteristic surface factor based on the surface modification of the surface with a mathematical approach. The novelty of this study was to prepare the novel CMC/Chitosan-α-Fe$_2$O$_3$ NPs coated 17–4 PH stainless-steel foam and investigate the surface characteristics of the coating. We investigated surface properties of the nanostructure and CMC/Chitosan-α-Fe$_2$O$_3$ NPs coated 17–4 PH stainless-steel foam using Brunauer–Emmett–Teller (BET), Scanning Electron Microscopy/Energy-Dispersive X-Ray Spectroscopy (SEM/EDX), X-Ray diffraction (XRD), and Fourier transform infrared spectroscopy (FT-IR) techniques and to compare the surface tensions of CMC/Chitosan-α-Fe$_2$O$_3$ NPs. The surface characterization results showed that the α-Fe$_2$O$_3$ NPs

had a spherical shape, nanosize (10–20 nm), large surface area (180.37 m^2/g) and homogeneous distribution in colloidal solutions. The surface tensions of CMC/Chitosan-α-Fe$_2$O$_3$ NPs were compared to determine the surface properties of the nanostructure as affected by the operating parameters such as the concentration (0–1 ppm), mass fraction (10–20%) of silica, mass fraction (1–5%) of cetyltrimethylammonium bromide (CTAB), temperature (25–45 °C), pH (3–10), sonication time (5–20 min), and the amplitude of sonication (10–40%). Furthermore, experimental results provided a mathematical model to describe the effect of CMC/Chitosan-α-Fe$_2$O$_3$ NPs on the surface tension for colloidal solutions. Error analysis is also conducted to assess the validity of the obtained models. According to previous reported studies, this study is the first report of the rheological properties of the CMC/Chitosan-α-Fe$_2$O$_3$ NPs as a coating biomaterial for foams under ultrasonic irradiation. As far as we know, the coating of CMC/Chitosan-α-Fe$_2$O$_3$ NPs on the pore channels of 17–4 PH stainless-steel foam has not been reported. For the first time, a mathematical model was formulated to determine the change in surface tension of α-Fe$_2$O$_3$ NPs for homogeneous coating process. This novel nanomaterial can be a candidate for to be used as a new implant with excellent surface property in bone tissue engineering applications. Consequently, we have suggested that CMC/Chitosan-α-Fe$_2$O$_3$ NPs has a great potential for designing a promising nanomaterial for biomedical applications.

Materials and methods

Materials

Iron (III) chloride hexahydrate (FeCl$_3$·6H$_2$O) (≥99%), chitosan (low molecular weight), chitosan (Mw: 50–190 kDa) and carboxymethyl cellulose (CMC) (Mw: 250 kDa, high viscosity, the degree of substitution: 0.90) were purchased from Sigma-Aldrich Company (Germany). Polyvinyl alcohol (PVA), carbamide particles (CO(NH$_2$)$_2$), sodium borohydride (NaBH$_4$), ethyl alcohol (C$_2$H$_5$OH), and silica gel (SiO$_2$) (pore size 60 Å, 70–230 mesh), acetic acid (glacial, 100%), NaOH (>99% purity), and cetyltrimethylammonium bromide (CTAB) (Average mass: 364.448 Da) were purchased from Merck Company. 17–4 PH stainless-steel powder was purchased from Carpenter Company (Sweden). The chemical composition of 17–4 PH stainless-steel powder was presented in Table 1. All chemicals and reagents were analytical grade and used without further purification.

Characterization part

Characterization of the CMC/Chitosan-α-Fe$_2$O$_3$ NPs

The surface morphology of all samples was investigated using a scanning electron microscope (SEM, Quanta FEG 450). An X-ray diffractometer (Bruker D8 Advance X-ray Diffractometer) was used (Cu Kα, $\lambda = 0.15418$ nm, 40 kV, 40 mA, 2θ angles

Table 1 Chemical composition of 17–4 PH stainless-steel powder

Element	%
Cr	15.18
Ni	4.470
Cu	3.470
Mn	0.650
Si	0.380
Nb + Ti	0.200
Mo	0.150
S	0.030
C	0.020
P	0.016
Fe	Balance

from 2 to 75 with a step size of 0.02°/s). FTIR spectroscopy was recorded using the Perkin Elmer FTIR emission spectrometer (Spectrum Two) with KBr powder (4000–600 cm^{-1} frequency range with a resolution of 4 cm^{-1} and 8 scans). Measurements of surface tension of all colloidal solutions were performed with a force tensiometer (K11, KRUSS, Germany) at 25 ± 0.5 °C.

Characterization of the uncoated and coated 17–4 PH stainless-steel foams with CMC/Chitosan-α-Fe$_2$O$_3$ NPs

The density and porosity content of sintered 17–4 PH stainless-steel foam were determined using Archimedes' principle in a Sartorius precision balance equipped with a density determination kit. Mechanical properties of the specimens were studied by the compression test performed on a Zwick–Roell Z050 materials testing machine. The surface roughness of the uncoated and coated 17–4 PH stainless-steel foams with CMC/Chitosan-α-Fe$_2$O$_3$ NPs was measured using a Surftest 210 type Mitutoyo surface profilometer (Mitutoyo, Japan) (5 µm tip radius). The arithmetic average of the surface roughness (Ra) was achieved by significantly bigger than the pores with a chisel point pen to eliminate the effects of pore size change on the measurements. The thickness of the coatings was examined using optical microscope (Nikon ME600). The pores of the steel foam were filled with a cold-hardening epoxy resin and then etched in 2% Nital solution for optical analysis.

Preparation of the CMC/Chitosan-α-Fe$_2$O$_3$ NPs

The CMC/Chitosan-α-Fe$_2$O$_3$ NPs were prepared following the procedure described in our previous paper [21]. A solution of FeCl$_3$·6H$_2$O (0.54 g/30 mL) in a mixture of 24 mL ethanol/6 mL of distilled water was dissolved at 25 °C. 0.1 M NaBH$_4$ and FeCl$_3$·6H$_2$O solutions were mixed then it was stirred vigorously under nitrogen gas atmosphere for 15 min. 0.1 g of CMC was dissolved in 100 mL of distilled water for 24 h, and 0.05 g of chitosan was dissolved in 50 mL 2% (v/v) glacial acetic solution

for 30 min. Then, the CMC and chitosan solutions were mixed, and 0.02 g of silica was added in 100 mL water. All solutions were mixed and sonicated for 10 min at room temperature under nitrogen gas atmosphere. Finally, the synthesized CMC/Chitosan-α-Fe_2O_3 NPs were stored at 25 °C until further use.

Preparation of 17–4 PH stainless-steel foam

17–4 PH stainless-steel foam as the substrate material was produced by the space holder-water leaching technique in powder metallurgy. This technique involved four main stages: powder mixing, compaction, removal of space holder by water leaching, and sintering.Initially, 2.5 g of PVA was dissolved in 97.5 mL of distilled water. 250 g of steel powder was added to PVA solution. The blend was mixed for 30 min. Then, 20 g of blend was mixed with 80 g of irregular shaped carbamide particles (710–1000 μm) in a Turbula type mixer for 60 min. The mixture was compacted uniaxially at 200 MPa in a steel die using a hydraulic press into cylindrical specimens with a diameter of 10 mm and heights of 15 mm. The green steel foams were immersed in distilled water at room temperature to leach the space holder. The PVA in the green specimens was thermally removed as part of sintering cycle, which consisted of heating at a ramp rate of 5 °C/min to 410 °C (debinding) with a dwell time of 40 min, followed by heating at rate of 10 °C/min to sintering temperatures. The steel foams were sintered at 1260 °C for 40 min under high purity hydrogen gas atmosphere in a horizontal tube furnace.

Coating process of CMC/Chitosan-α-Fe_2O_3 NPs/17–4 PH stainless-steel foam

For the coating process, the cylindrical foam samples were cut into slices with a small diameter (⌣0.5 cm) by EDM (Electrical Discharge Machining) with process parameters such as peak current: 3 A, pulse-on time: 50 μs, pulse-of time: 30 μs, open circuit voltage: 60 V, and wire feed speed: 5 m/s. CuZn37 master brass wire with 0.15 mm diameter (900 N/mm^2 tensile strength). After the cutting step, the dust was removed from the sample surface with compressed air. The uncoated 17–4 PH stainless-steel foam was immersed in the coating α-Fe_2O_3 NPs solution in a direction perpendicular, kept in the solution for 5 min at room temperature. The sample was dried at 50 °C with a 30% relative humidity for 3 h. Based on weight difference results of the uncoated foam before and after coating, 3.3 mg of solution was loaded on the foam.

Surface tension measurement of CMC/Chitosan-α-Fe_2O_3 NPs

In this study, applying a force tensiometer, the surface tensions of all colloidal solutions were measured at 25 ± 0.5 °C. The measuring error and measurement range were 0.1 mN/m and 0.000015–0.0001 mN/m, respectively. To calibrate the system, the surface tension of distilled water was measured at 25 °C. We focused on the operating parameters such as the mass fraction (1–10%) of silica, the concentration (0–1 ppm) of solutions, sonication time (1–15 min), the amplitude of sonication

(10–40%), and temperature (25–45 °C) on the surface tensions of synthesized nanoparticles and results were compared to design a promising nanomaterial for biomedical applications.

Construction of mathematical model

Critical micelle concentrations are obtained for each mass fraction (10%, 15%, and 20%) of silica by intersecting the lines, which are obtained by linear regressions applied to the decreasing and stable part of the concentration data [22]. A mathematical model for surface tension is also obtained as a function of the operating variables, namely, concentration, mass fraction of silica, mass fraction of CTAB, temperature, pH, sonication time, and amplitude of sonication. In order to obtain such a model, first an exponential regression is applied to the concentration surface tension data corresponding to concentration, for each mass fraction (10, 15, and 20%) of silica. The R^2 values of these regressions are computed as 0.958, 0.988, and 0.985, respectively. Then, another exponential regression is applied to the surface tension data corresponding to temperature ($R^2 = 0.997$). Linear regressions are conducted for pH, sonication time and surface tension data corresponding to mass fraction of CTAB, and linear relations are obtained for the stated variables with R^2 values of 0.955, 0.971, 0.915, respectively. For modeling of amplitude of sonication, a logistic regression is performed ($R^2 = 0.985$). Then, the equations obtained using regressions are normalized with respect to the fixed parameters in the surface tension data corresponding to concentration. The values of these fixed parameters are 25 °C (temperature), 5 (pH), 20 min (sonication time), 5% (mass fraction of CTAB), and 40% (amplitude). After the normalization of equations for each operating parameter, all functions reconstructed have been multiplied by the exponential function of surface tension data corresponding to concentration for each mass fraction of silica.

Error analysis methods

In this study, we used four different error analysis methods such as the sum of squares of errors (SSE), the hybrid fractional error function (HYBRID), Marquart's percentage standard deviation (MPSD), and the average relative error (ARE) all expressions were given in Table 2 [23–26]. Where, γ_e: experimental surface

Table 2 The error analysis methods

Expressions	Error analysis methods	References
$\sum_{i=1}^{n} (\gamma_{cal} - \gamma_e)^2{}_i$	SSE	[23]
$\frac{100}{n-p} \sum_{i=1}^{n} \left[\frac{(\gamma_e - \gamma_{cal})^2{}_i}{\gamma_e} \right]$	HYBRID	[24]
$100 \sqrt{ \frac{1}{n-p} \sum_{i=1}^{n} \left(\frac{\gamma_e - \gamma_{cal}}{\gamma_e} \right)^2_i }$	MPSD	[25]
$\frac{100}{n-p} \sum_{i=1}^{n} \left| \frac{\gamma_e - \gamma_{cal}}{\gamma_e} \right|_i$	ARE	[26]

tension, γ_{cal}: calculated surface tension, n: number of data points and p: number of parameters.

Results and discussion

Characterization of 17–4 PH stainless-steel foam

The photograph of the sintered stainless-steel foam and SEM image of stainless-steel foam were shown in Fig. 1a and b, respectively. The specimens had a relatively uniform distribution of pores. Cell walls separating each pore from its neighbors were clearly seen. No cracks were observed in the highly porous structures, but large numbers of micropores were formed in the cell walls. Although the macropores in foams appear to be isolated from each other, they were in fact connected owing to the micropores in the cell walls. In spite of sintering between steel particles, the macroporous structure remained with a small shrinkage. This suggested that the pore structures could be designed by using morphological properties such as proper size, shape and content of the carbamide particles.

Total porosity and pore size had a critical role in tissue ingrowth into the implant. The minimum pore size was considered to be 100 mm and larger pore size results in greater tissue ingrowth. In the case of pores with size less than 100 mm, cells did not grow into the pores because of spanning of pores by the cells. The morphology of the final pores of the sintered 17–4 PH stainless-steel foams replicated the initial shape of the carbamide particles that were used as space holder. In this study, the total porosity of the specimen consisted of about 58% open and 14% closed porosity.

The mean size and the mean sphericity of the pores were determined to be 620 μm and 0.58, respectively. These values for carbamide particles were determined to be 780 μm and 0.64, respectively. The decrease in the size and sphericity was attributed to crushing of the carbamide particles during pressing and moistening before mixing. Compression tests were conducted on the foam to evaluate their elastic and
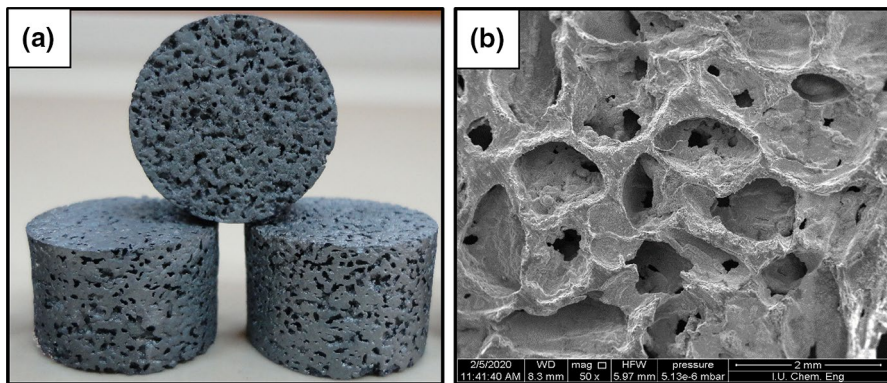

Fig. 1 **a** The photograph of stainless-steel foam and **b** SEM image of stainless-steel foam

plastic deformation behavior. The compressive yield strength and Young's modulus of 17–4 PH stainless-steel foam were 48 MPa and 0.51 GPa, respectively. Compressive yield strength and Young's modulus of cancellous bone are 40–150 MPa and 0.09–1.5 GPa, respectively [27]. As a result, mechanical properties of the 17–4 PH stainless-steel foams were close to cancellous bones. The average surface roughness value of uncoated steel foam was measured in the range of 3.98–4.25 μm. As known, these optimum parameters (surface roughness, mean size and sphericity values of the pores) are suitable for biomedical applications [27].

Characterization of α-Fe$_2$O$_3$ NPs and α-Fe$_2$O$_3$ NPs coated 17–4 PH stainless-steel foam

In this study, the synthesized CMC/Chitosan-α-Fe$_2$O$_3$ NPs were used in the first time as a green coating material for 17–4 PH stainless-steel foam. There have been several reported studies on the enhanced surface properties of stainless-steel foam and improving the biocompatibility of the stainless-steel foams, but limited studies have been reported on surface properties of NPs coated stainless-steel foam [28–32]. The surface morphologies of the 17–4 PH stainless-steel foam and CMC/Chitosan-α-Fe$_2$O$_3$ NPs coated 17–4 PH stainless-steel foam in Fig. 2a and b. EDX image of CMC/Chitosan-α-Fe$_2$O$_3$ NPs was given in Fig. 2c. In Fig. 2, the surface morphology results showed the treated surface of 17–4 PH stainless-steel foam was completely covered with CMC/Chitosan-α-Fe$_2$O$_3$ NPs and CMC/Chitosan-α-Fe$_2$O$_3$ NPs were uniformly dispersed in the CMC/Chitosan@silica [33]. The average particle size of CMC/Chitosan-α-Fe$_2$O$_3$ NPs was 10–20 nm with a spherical shape. According to BET results, the surface area of CMC/Chitosan-α-Fe$_2$O$_3$ NPs was measured 180.37 m^2/g.

The average surface roughness value of the CMC/Chitosan-α-Fe$_2$O$_3$ NPs coated steel foam was measured in the range of 4.59–5.91 μm. The coating thickness values were measured using an optical microscope in the range of 15 and 30 μm closer view of pore walls of coated steel foams were observed in Fig. 3 and it was clear that there were micropores obvious in the cell walls. The coating thickness values were measured using an optical microscope in the range of 10 and 20 μm. In this study, we observed that the coating process of stainless-steel foam was effective and there were no cracks or delamination was observed along the interface. According to our experimental results, we demonstrated that the coating process had a major role in the surface and structural properties of the foam due to the changes in the morphology and surface roughness parameters.

In our previous study, X-ray powder diffraction (XRD) was used to identify the structural properties of α-Fe$_2$O$_3$ NPs and to determine the crystallinity of α-Fe$_2$O$_3$ NPs.

The XRD patterns of CMC/Chitosan-α-Fe$_2$O$_3$ NPs were given in Fig. 4. According to XRD results, the characteristic peaks of CMC/Chitosan-α-Fe$_2$O$_3$ NPs (2 theta: 31° and 45°) were observed. The FTIR spectra of the α-Fe$_2$O$_3$ NPs were given in Fig. 5. In our previous FTIR results, the characteristic peaks of CMC/Chitosan-α-Fe$_2$O$_3$ NPs were observed at 3479 cm^{-1} (–OH), 2924 cm^{-1} (–OH), 1750 cm^{-1} (C=O
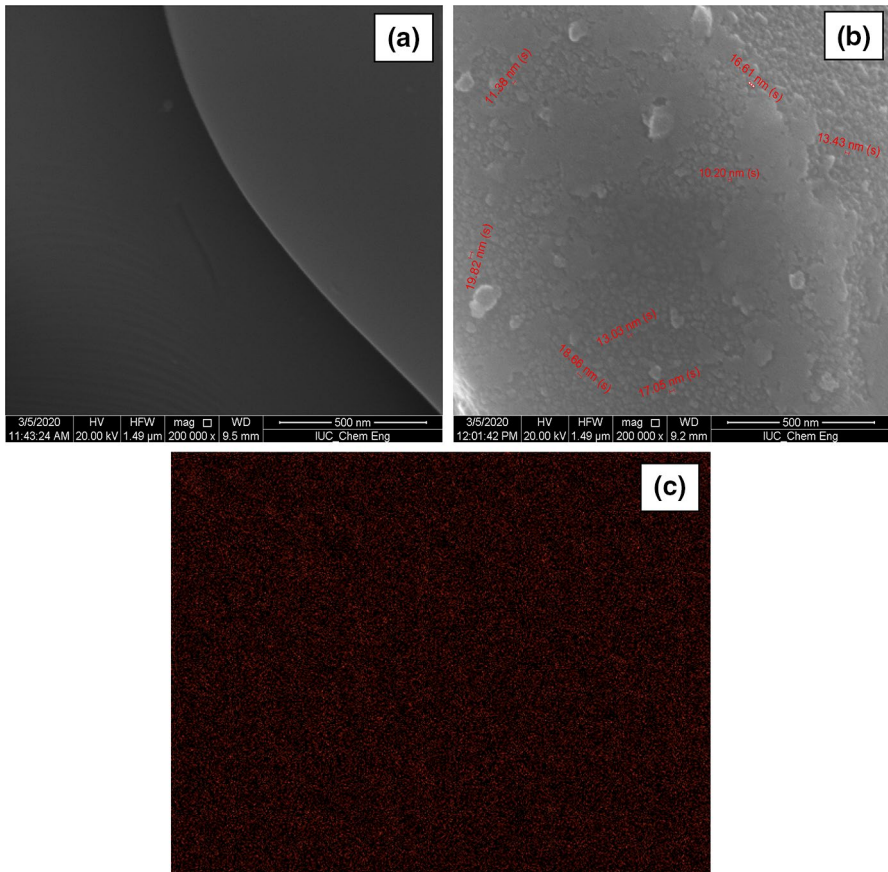
Fig. 2 SEM images of **a** 17–4 PH stainless-steel foam with × 200.000 magnification and **b** CMC/Chitosan-α-Fe$_2$O$_3$ NPs coated 17–4 PH stainless-steel foam with × 200.000 magnification **c** EDX images of CMC/Chitosan-α-Fe$_2$O$_3$ NPs

stretching), 1514 cm^{-1} (–NH), 1318 cm^{-1} (–CH$_2$OH) and at 530 cm^{-1} (α-Fe$_2$O$_3$) [21].

The measurement of surface tension of the CMC/Chitosan-α-Fe$_2$O$_3$ NPs

There have been limited studies on the surface tension of the synthesized nano-structures [34–36]. In this study, we focused on the effect of the mass fraction (1–10%) of silica, the concentration (0–1 ppm) of solutions, sonication time (1–15 min), the amplitude of sonication (10–40%), and temperature (25–45 °C) on the surface tension of CMC/Chitosan-α-Fe$_2$O$_3$ NPs solutions were shown in Figs. 6 and 7. The surface tension of NPs /water from 47.83 to 36.22 mN/m by changing the concentration of colloidal solutions in a range of 0–0.05 ppm (pressure: 1 atm, temperature: 25 °C) was measured (Fig. 4). We investigated
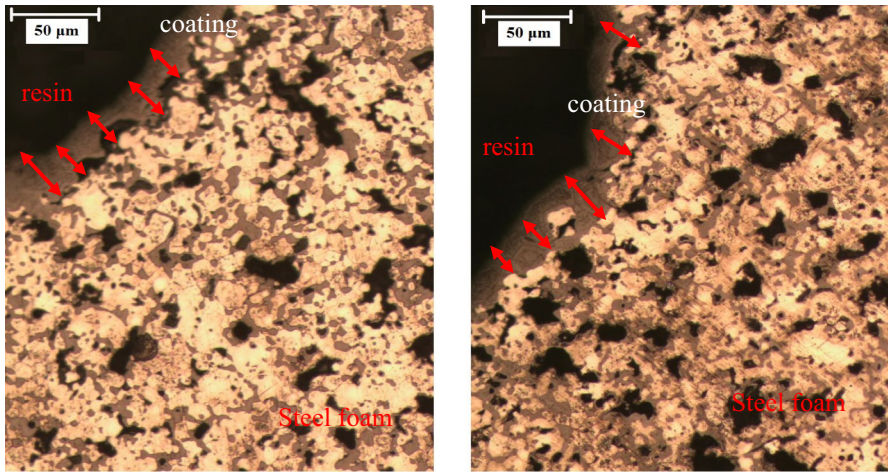
Fig. 3 Cross-sectional surface microstructure of pore wall of the CMC/Chitosan-α-Fe$_2$O$_3$ NPs coating on steel foams
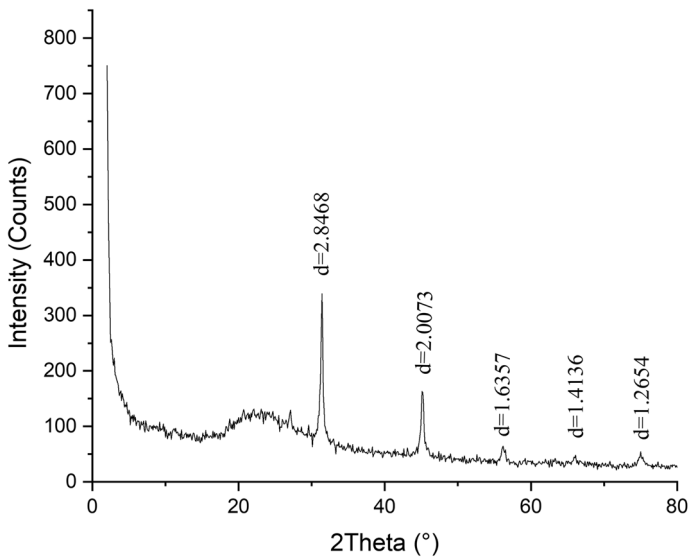

Fig. 4 XRD analysis of the CMC/Chitosan-α-Fe$_2$O$_3$ NPs

the effect of the mass fraction on the NPS/water nanofluid behavior based on the surface tension and found that there was a relationship between the additive functions of the systems and the surface tension using a mathematical model (Figs. 6 and 7). According to results, the surface tension of α-Fe$_2$O$_3$ NPs/water was increased with the increase in the concentration of α-Fe$_2$O$_3$ NPs [37]. There have been few studies reported on a mathematical approach to evaluate the
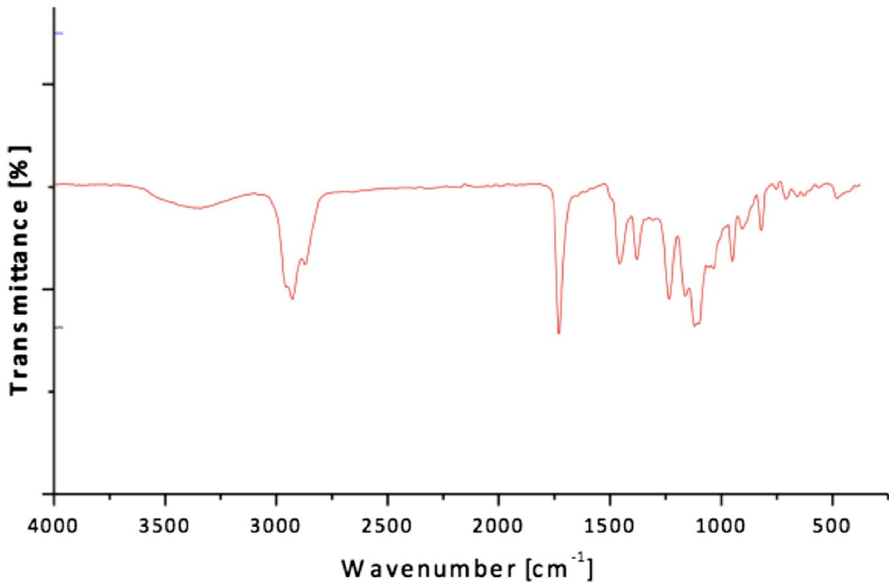
Fig. 5 FTIR analysis of the CMC/Chitosan-α-Fe$_2$O$_3$ NPs

effects of the sonication inputs such as time, power, and amplitude on the nano-system formation and stabilization based on surface tension behaviors [38]. We showed that the sonication method reduced the surface tension and improved the stability of colloidal solutions. Also, we observed that surface tension results, and surface analysis results were compatible. The effect of temperature (25–45 °C) on the surface tension of α-Fe$_2$O$_3$ NPs/water system (the interface between NPs and water phase) was proven. The results showed that the temperature was increased, and the surface tension decreased as the attraction forces between the particles decreased [38]. The novelty of this study was that it had a large amount of data on the surface tension of NPs/water system, a mathematical relationship was established between the values of the inputs (mass fraction, concentration, sonication time and amplitude) and the output (surface tension) and all parameters was used to fit the equation for the surface tension of nano-particles [39–41].

Determination of critical micelle concentrations

Critical micelle concentrations are determined by intersecting the lines, which are obtained by linear regressions applied to the decreasing and stable part of the data. The critical micelle concentrations were found to be 0.399, 0.428, and 0.573 ppm for mass fractions of 10, 15 and 20% silica, respectively (Fig. 6). The experimental data are available in the Supplementary Materials.
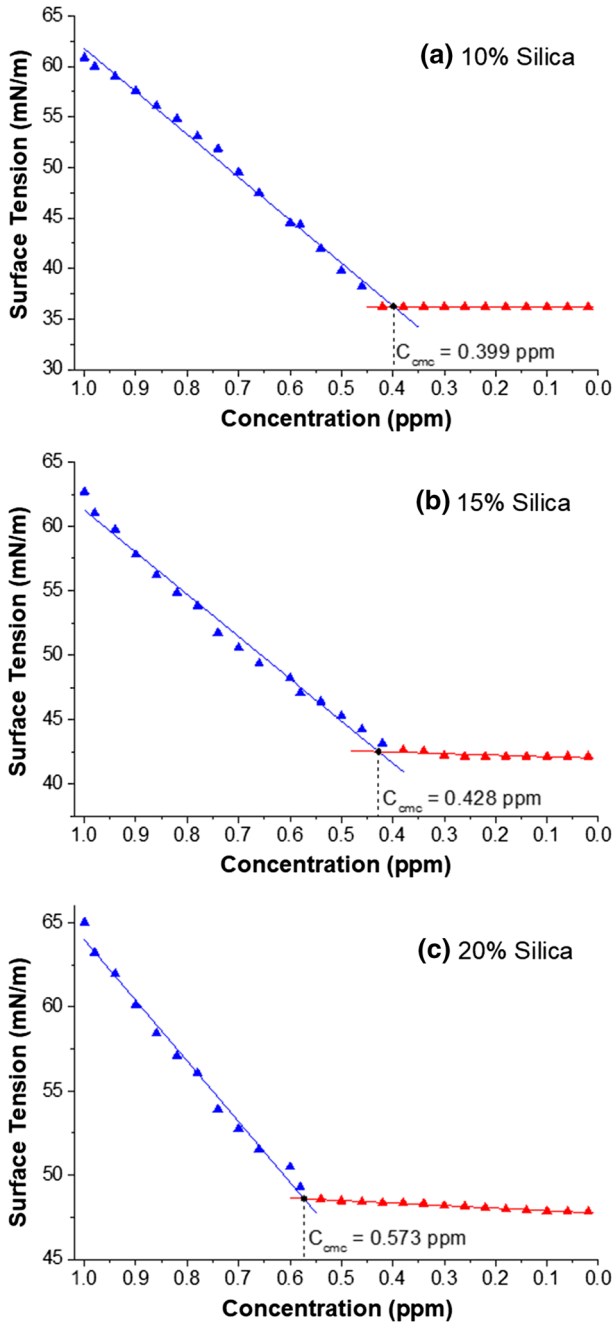
Fig. 6 Determination of critical micelle concentrations for 10% (**a**), 15% (**b**), 20% (**c**) mass fractions of silica
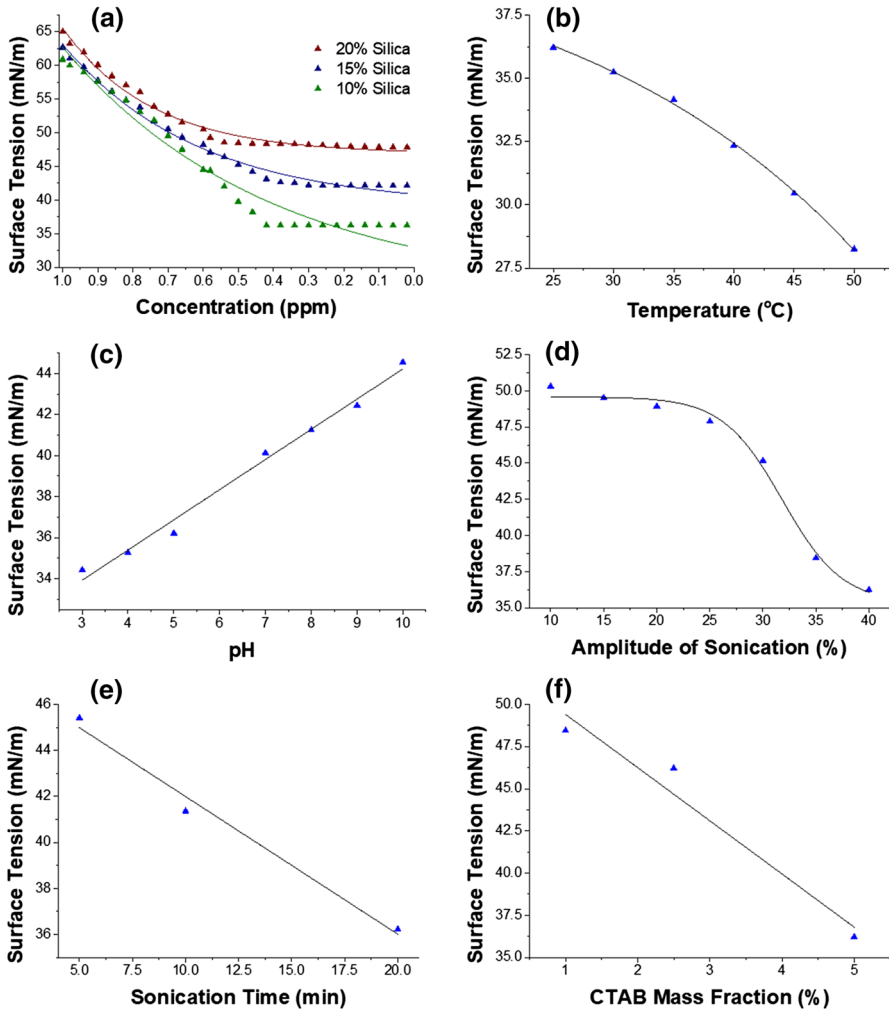
Fig. 7 The effects of concentration for each mass fraction of silica (**a**), temperature (**b**) pH (**c**), amplitude of sonication (**d**), sonication time (**e**) and mass fraction of CTAB (**f**) on surface tension of α-Fe$_2$O$_3$ NPs/ water system

Modeling of surface tension

In this study, we have obtained surface tension as a function of operating variables concentration (C), temperature (T), pH, amplitude of sonication (AMP), sonication time (t_s), and mass fraction of CTAB (m_{CTAB}) for each mass fraction (10, 15, and 20%) of silica. Firstly, an exponential regression is applied to the surface tension data corresponding to the concentration, while the remaining variables are kept constant at $T=25$ °C, pH=5, AMP=40%, $t_s=20$ min, and $m_{CTAB}=5\%$. As a result of these regressions, the functions of $\gamma_{C10}(C)$ Eq. 3.1, $\gamma_{C15}(C)$ Eq. 3.2, and $\gamma_{C20}(C)$ Eq. 3.3 are provided for mass

fraction of 10%, 15%, and 20% silica, respectively. These functions are illustrated with the experimental data (see Supplementary Materials) in Fig. 7a.

$$\gamma_{C10}(C) = 26.31286 + 6.64406e^{\frac{C}{0.5880114}} \tag{3.1}$$

$$\gamma_{C15}(C) = 39.08639 + 1.80472e^{\frac{C}{0.3861944}} \tag{3.2}$$

$$\gamma_{C20}(C) = 46.86883 + 0.3793e^{\frac{C}{0.2566275}} \tag{3.3}$$

Then, regressions are applied to the surface tension data corresponding to temperature, pH, amplitude of sonication, sonication time, and mass fraction of CTAB respect to fixed parameters given in Table 3 (Eqs. 3.3–3.8). Thus, equations in Table 3 are obtained and all functions and the experimental data (see Supplementary Materials) are illustrated in Fig. 7.

After obtaining Eqs. 3.4–3.8, the functions $\gamma_T(T)$, $\gamma_{pH}(pH)$, $\gamma_{AMP}(AMP)$, $\gamma_{ts}(t_S)$, and $\gamma_{m_{CTAB}}(m_{CTAB})$ are normalized as in Eqs. 3.9–3.14, respectively. The normalization is performed in a way that the normalized functions result 1 at fixed parameters $T = 25$ °C, pH$=5$, AMP$=40\%$ min, $t_s = 20$ min, and $m_{CTAB} = 5\%$.

$$\gamma_{TN}(T) = \frac{\gamma_T(T)}{\gamma_T(25)} = 1.12477 - 0.045384e^{0.040772T} \tag{3.9}$$

$$\gamma_{pHN}(pH) = \frac{\gamma_{pH}(pH)}{\gamma_{pH}(5)} = 0.039915pH + 0.80043 \tag{3.10}$$

$$\gamma_{AMPN}(AMP) = \frac{\gamma_{AMP}(AMP)}{\gamma_{AMP}(40)} = 0.97924 + \frac{0.39563}{1 + e^{0.35426AMP - 11.27723}} \tag{3.11}$$

$$\gamma_{tsN}(t_S) = \frac{\gamma_{ts}(t_S)}{\gamma_{ts}(20)} = -0.016623t_s + 1.33246 \tag{3.12}$$

Table 3 Equations via experimental fixed operating parameters of α-Fe$_2$O$_3$ NPs

Equations	Eq. #	Experimental operating parameters					
		C (ppm)	T (°C)	pH	AMP (%)	t_s (min)	m_{CTAB} (%)
$\gamma_T(T) = 40.84154 - 4.5406e^{\frac{T-24.8807}{24.5269}}$	(3.1)	0.42	–	5	40	20	5
$\gamma_{pH}(pH) = 1.47174pH + 29.51358$	(3.2)	0.42	25	–	40	20	5
$\gamma_{AMP}(AMP) = 35.3128 + \frac{49.57974 - 35.3128}{1+e^{\frac{AMP-31.83292}{2.82276}}}$	(3.3)	0.42	25	5	–	20	5
$\gamma_{ts}(t_S) = -0.59857t_s + 47.98$	(3.4)	0.42	25	5	40	–	5
$\gamma_m(m_{CTAB}) = -3.15327m_{CTAB} + 52.56092$	(3.5)	0.42	25	5	40	20	–

$$\gamma_{mN}(m_{CTAB}) = -\frac{\gamma_m(m_{CTAB})}{\gamma_m(5)} = -0.085312 m_{CTAB} + 1.42656 \qquad (3.13)$$

Finally, multiplying all normalized functions by $\gamma_{C10}(C)$, $\gamma_{C15}(C)$, and $\gamma_{C20}(C)$; we obtain the surface tension as a function of the operating variables for mass fractions of 10%, 15%, and 20% silica, respectively Eqs. 3.14–3.16.

$$\gamma_{10\%}(T, pH, AMP, t_s, m_{CTAB}, C) = \gamma_{TN}(T)\gamma_{pHN}(pH)\gamma_{AMPN}(AMP)\gamma_{tsN}(t_S)\gamma_{mN}(m_{CTAB})\gamma_{C10}(C)$$
$$(3.14)$$

$$\gamma_{15\%}(T, pH, AMP, t_s, m_{CTAB}, C) = \gamma_{TN}(T)\gamma_{pHN}(pH)\gamma_{AMPN}(AMP)\gamma_{tsN}(t_S)\gamma_{mN}(m_{CTAB})\gamma_{C15}(C)$$
$$(3.15)$$

$$\gamma_{20\%}(T, pH, AMP, t_s, m_{CTAB}, C) = \gamma_{TN}(T)\gamma_{pHN}(pH)\gamma_{AMPN}(AMP)\gamma_{tsN}(t_S)\gamma_{mN}(m_{CTAB})\gamma_{C20}(C)$$
$$(3.16)$$

Error analysis

In this study, we investigated the effects of ultrasonic cavitation on surface morphology evolution of NPs. Also, the successful optimization strategy of NPs was experimentally designed with different operating parameters (ultrasonic irradiation inputs) using the mathematical model with to the surface tension data. Additionally, we highlighted that the interaction of the water with NPs under ultrasonic irradiation plays a major role in modulating particle size and distribution due to performance of physicochemical properties.

Also, we conducted an error analysis for functions obtained in Eqs. 3.14–3.16 in order to evaluate the performance of the obtained models. SSE, HYBRID, MPSD and ARE values for each function are determined by comparing the results of each equation with 104 experimental data points. The results were given in Table 4 and the schematic diagram of the experimental procedure was given in Fig. 8. By applying Eqs. 3.14–3.16, we compared in terms of accuracy, it is seen that Eq. 3.16 (20% silica) represents the experimental data the best. While the absolute error is relatively higher in Eq. 3.14 (10% silica), the similarity in MPSD value suggests that the standard deviation percentage is similar for each relation. These error values provide a reference for the modeling of surface tension with respect to similar operating variables.

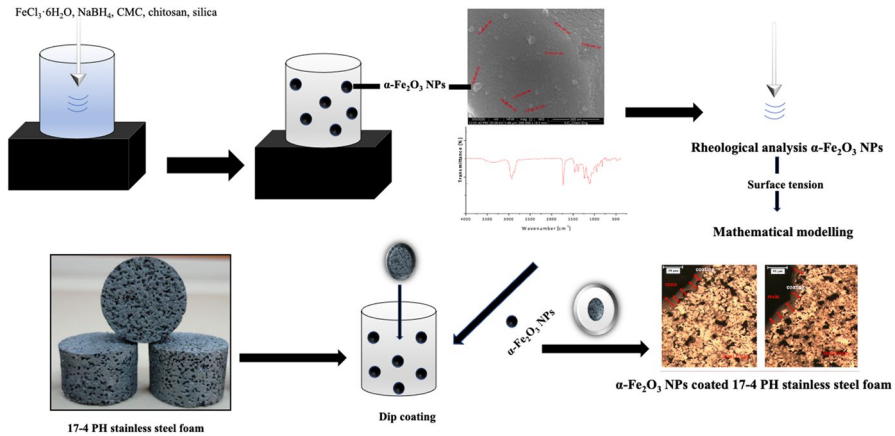| Table 4 Error analysis results of mathematical models for CMC/Chitosan-α-Fe$_2$O$_3$ NPs		10% Silica	15% Silica	**20% Silica**
	SSE	433.3011	76.93431	**46.91477**
	HYBRID	10.40619	1.669168	**0.911355**
	MPSD	92.78478	90.64954	**90.32642**
	ARE	4.462957	1.620021	**1.152615**

Fig. 8 The schematic diagram of the experimental procedure

Conclusion

In this study, preparation, characterization and surface properties of the synthesized CMC/Chitosan-α-Fe_2O_3 NPs and CMC/Chitosan-α-Fe_2O_3 NPs coated 17–4 PH stainless-steel foam were investigated. Surface tension behaviors of CMC/Chitosan-α-Fe_2O_3 NPs were experimentally determined as a function of the operating parameters. The influence of CMC/Chitosan-α-Fe_2O_3 NPs coating on morphology properties of 17–4 PH stainless-steel foam was performed. This study proposed a mathematical model to determine the change in surface tension of NPs for homogeneous coating process. Our research model presented as a methodological prediction, which explains the relation between surface tension and operating parameters using different error analysis methods with minimum error values. The novel CMC/Chitosan-α-Fe_2O_3 NPs coated 17–4 PH stainless-steel foam is a candidate nanomaterial for biomedical applications.

Declarations

Conflict of interest The authors declare no conflict of interests.

References

1. Israel LL, Galstyan A, Holler E, Ljubimova JY (2020) Magnetic iron oxide nanoparticles for imaging, targeting and treatment of primary and metastatic tumors of the brain. J Control Release 320:45–62. https://doi.org/10.1016/j.jconrel.2020.01.009

2. Phul R, Shrivastava V, Farooq U, Sardar M, Kalam A, Al-Sehemi AG, Ahmad T (2019) One pot synthesis and surface modification of mesoporous iron oxide nanoparticles. Nano-Struct Nano-Objects 19:100343. https://doi.org/10.1016/j.nanoso.2019.100343

3. Gupta AK, Gupta M (2005) Synthesis and surface engineering of iron oxide nanoparticles for biomedical applications. Biomaterials 26(18):3995–4021. https://doi.org/10.1016/j.biomaterials.2004.10.012

4. Alphandéry E (2020) Iron oxide nanoparticles for therapeutic applications. Drug Discovery Today 25(1):141–149. https://doi.org/10.1016/j.drudis.2019.09.020

5. Guo L, Chen H, He N, Deng Y (2018) Effects of surface modifications on the physicochemical properties of iron oxide nanoparticles and their performance as anticancer drug carriers. Chin Chem Lett 29(12):1829–1833. https://doi.org/10.1016/j.cclet.2018.10.038

6. Navarro-Palomares E, González-Saiz P, Renero-Lecuna C, Martín-Rodríguez R, Aguado F, González-Alonso D, Barquín LF, González J, López MB, Valiente R (2020) Dye-doped biodegradable nanoparticle SiO 2 coating on zinc-and iron-oxide nanoparticles to improve biocompatibility and for in vivo imaging studies. Nanoscale 12(10):6164–6175. https://doi.org/10.1039/c9nr08743e

7. Ali I (2018) Microwave assisted economic synthesis of multi walled carbon nanotubes for arsenic species removal in water: batch and column operations. J Mol Liq 71:677–685. https://doi.org/10.1016/j.molliq.2018.09.021

8. Burakova EA, Dyachkova TP, Rukhov AV, Tugolukov EN, Galunin EV, Tkachev AG, Ali I (2018) Novel and economic method of carbon nanotubes synthesis on a nickel magnesium oxide catalyst using microwave radiation. J Mol Liq 253:340–346. https://doi.org/10.1016/j.molliq.2018.01.062

9. Ali I, Suhail M, Alothman ZA, Alwarthan A (2018) Recent advances in syntheses, properties and applications of TiO$_2$ nanostructures. RSC Adv 8(53):30125–30147. https://doi.org/10.1039/c8ra06517a

10. Ali I, Alharbi OM, Alothman ZA, Alwarthan A (2018) Facile and eco-friendly synthesis of functionalized iron nanoparticles for cyanazine removal in water. Coll Surf B Biointerfaces 171:606–613. https://doi.org/10.1016/j.colsurfb.2018.07.071

11. Ali I, Kucherova A, Memetov N, Pasko T, Ovchinnikov K, Pershin V, Kuznetsov D, Galunin E, Grachev V, Tkachev A (2019) Advances in carbon nanomaterials as lubricants modifiers. J Mol Liq 279:251–266. https://doi.org/10.1016/j.molliq.2019.01.113

12. Ali I, Alharbi OM, Alothman ZA, Badjah AY (2018) Kinetics, thermodynamics, and modeling of amido black dye photodegradation in water using Co/TiO$_2$ nanoparticles. Photochem Photobiol 94(5):935–941. https://doi.org/10.1111/php.12937

13. Lassoued A, Dkhil B, Gadri A, Ammar S (2017) Control of the shape and size of iron oxide (α-Fe$_2$O$_3$) nanoparticles synthesized through the chemical precipitation method. Results Phys 7:3007–3015. https://doi.org/10.1016/j.rinp.2017.07.066

14. Meyerstein D, Adhikary J, Burg A, Shamir D, Albo Y (2020) Zero-valent iron nanoparticles entrapped in SiO$_2$ sol-gel matrices: a catalyst for the reduction of several pollutants. Catal Commun 133:105819. https://doi.org/10.1016/j.catcom.2019.105819

15. Dolores R, Raquel S, Adianez GL (2015) Sonochemical synthesis of iron oxide nanoparticles loaded with folate and cisplatin: effect of ultrasonic frequency. Ultrason Sonochem 23:391–398. https://doi.org/10.1016/j.ultsonch.2014.08.005

16. Ahmed N, Ahmad NM, Fessi H, Elaissari A (2015) In vitro MRI of biodegradable hybrid (iron oxide/polycaprolactone) magnetic nanoparticles prepared via modified double emulsion evaporation mechanism. Colloids Surf B 130:264–271. https://doi.org/10.1016/j.colsurfb.2015.04.022

17. Szewczyk-Nykiel A (2014) The effect of the addition of boron on the densification, microstructure and properties of sintered 17–4 PH stainless steel. Czasopismo Techniczne 13:85–96. https://doi.org/10.4467/2353737XCT.14.293.3381

18. Zhang Q, Hu Z, Su W, Zhou H, Liu C, Yang Y, Qi X (2017) Microstructure and surface properties of 17–4PH stainless-steel by ultrasonic surface rolling technology. Surf Coat Technol 321:64–73. https://doi.org/10.1016/j.surfcoat.2017.04.052

19. Gu H, Gong H, Pal D, Rafi K, Starr T, Stucker B (2013) Influences of energy density on porosity and microstructure of selective laser melted 17–4PH stainless steel. In 2013 Solid Freeform Fabrication Symposium.

20. Vieira MT, Martins AG, Barreiros FM, Matos M, Castanho JM (2008) Surface modification of stainless-steel powders for microfabrication. J Mater Process Technol 201:651–656. https://doi.org/10.1016/j.jmatprotec.2007.11.162

21. Karakus S, Ilgar M, Tan E, Kilislioglu A (2018) Sonochemical preparation of α-Fe2 O3 nanoparticles in a dual biopolymer matrix. Curr Trends Chem Eng Process Technol. DOI: 10.29011. CTCEPT-107/100007

22. Le TTY, Hussain S, Lin SY (2019) A study on the determination of the critical micelle concentration of surfactant solutions using contact angle data. J Mol Liq 294:111582. https://doi.org/10.1016/j.molliq.2019.111582

23. Demirbas E, Kobya M, Konukman AES (2008) Error analysis of equilibrium studies for the almond shell activated carbon adsorption of Cr (VI) from aqueous solutions. J Hazard Mater 154(1–3):787–794. https://doi.org/10.1016/j.jhazmat.2007.10.094

24. Kapoor A, Yang RT (1989) Correlation of equilibrium adsorption data of condensible vapours on porous adsorbents. Gas Sep Purif 3(4):187–192. https://doi.org/10.1016/0950-4214(89)80004-0

25. Paluri P, Ahmad KA, Durbha KS (2020) Importance of estimation of optimum isotherm model parameters for adsorption of methylene blue onto biomass derived activated carbons: comparison between linear and non-linear methods. Biomass Conv Biorefinery. https://doi.org/10.1007/s13399-020-00867-y

26. Karakuş S (2019) A novel ZnO nanoparticle as drug nanocarrier in therapeutic applications: kinetic models and error analysis. J Turk Chem Soc Sect A Chem 6(2):119–132. https://doi.org/10.18596/jotcsa.405505

27. Matsushita T, Fujibayashi S, Kokubo T (2017) Titanium foam for bone tissue engineering. In: Metallic Foam Bone, 1st edn. Woodhead Publishing, pp 111–130. https://doi.org/10.1016/B978-0-08-101289-5.00004-4

28. Halim FSA, Chandren S, Nur H (2020) Carbon-containing-titania coated stainless-steel prepared by high voltage powder spray coating and its adhesion phenomena. Prog Org Coat 147:105782. https://doi.org/10.1016/j.porgcoat.2020.105782

29. Tang S, Chang X, Li M, Ge T, Niu S, Wang D, Jiang Y, Sun S (2021) Fabrication of calcium carbonate coated-stainless-steel mesh for efficient oil-water separation via bacterially induced biomineralization technique. Chem Eng J 405:126597. https://doi.org/10.1016/j.cej.2020.126597

30. Rezaei A, Golenji RB, Alipour F, Hadavi MM, Mobasherpour I (2020) Hydroxyapatite/hydroxyapatite-magnesium double-layer coatings as potential candidates for surface modification of 316 LVM stainless-steel implants. Ceram Int 46(16):25374–25381. https://doi.org/10.1016/j.ceramint.2020.07.005

31. Tran NG, Chun DM (2020) Simple and fast surface modification of nanosecond-pulse laser-textured stainless-steel for robust superhydrophobic surfaces. CIRP Ann 69(1):525–528. https://doi.org/10.1016/j.cirp.2020.04.012

32. Asl SM, Ganjali M, Karimi M (2019) Surface modification of 316L stainless-steel by laser-treated HA-PLA nanocomposite films toward enhanced biocompatibility and corrosion-resistance in vitro. Surf Coat Technol 363:236–243. https://doi.org/10.1016/j.surfcoat.2019.02.052

33. Gholipour-Ranjbar H, Ganjali MR, Norouzi P, Naderi HR (2016) Synthesis of cross-linked graphene aerogel/Fe2O3 nanocomposite with enhanced supercapacitive performance. Ceram Int 42(10):12097–12104. https://doi.org/10.1016/j.ceramint.2016.04.140

34. Gibson LJ, Ashby MF (1999) Cellular solids: structure and properties. Cambridge University Press, Cambridge

35. Gibson LJ (2005) Biomechanics of cellular solids. J Biomech 38(3):377–399. https://doi.org/10.1016/j.jbiomech.2004.09.027

36. Balla VK, Bodhak S, Bose S, Bandyopadhyay A (2010) Porous tantalum structures for bone implants: fabrication, mechanical and in vitro biological properties. Acta Biomater 6(8):3349–3359. https://doi.org/10.1016/j.actbio.2010.01.046

37. Huminic A, Huminic G, Fleaca C, Dumitrache F, Morjan I (2015) Thermal conductivity, viscosity and surface tension of nanofluids based on FeC nanoparticles. Powder Technol 284:78–84. https://doi.org/10.1016/j.powtec.2015.06.040

38. Cui Z, Chen J, Xue Y, Gan J, Chen X, Duan H, Zhang R, Liu J, Hao J (2020) Determination of surface tension and surface thermodynamic properties of nano-ceria by low temperature heat capacity. Fluid Phase Equilib 518:112627. https://doi.org/10.1016/j.fluid.2020.112627

39. Zhang S, Han X, Tan Y, Liang K (2018) Effects of hydrophilicity/lipophilicity of nano-TiO$_2$ on surface tension of TiO$_2$-water nanofluids. Chem Phys Lett 691:135–140. https://doi.org/10.1016/j.cplett.2017.11.005

40. Yan SR, Kalbasi R, Nguyen Q, Karimipour A (2020) Sensitivity of adhesive and cohesive intermolecular forces to the incorporation of MWCNTs into liquid paraffin: experimental study and modeling of surface tension. J Mol Liq 310:113235. https://doi.org/10.1016/j.molliq.2020.113235

41. Silva KCG, Sato ACK (2019) Sonication technique to produce emulsions: the impact of ultrasonic power and gelatin concentration. Ultrason Sonochem 52:286–293. https://doi.org/10.1016/j.ultsonch.2018.12.001

Publisher's Note Springer Nature remains neutral with regard to jurisdictional claims in published maps and institutional affiliations.

Authors and Affiliations

Selcan Karakuş[1] · İnci Albayrak[2] · Nuray Beköz Üllen[3] ⓘ · Mert Akin Insel[4] · Ayben Kilislioğlu[5]

1   Department of Chemistry, Faculty of Engineering, Istanbul University-Cerrahpasa, 34320 Istanbul, Turkey

2   Department of Mathematical Engineering, Yıldız Technical University, 34210 Avcilar, Istanbul, Turkey

3   Department of Metallurgical and Materials Engineering, Istanbul University-Cerrahpasa, 34320 Istanbul, Turkey

4   Department of Chemical Engineering, Yıldız Technical University, 34210 Istanbul, Turkey

5   Department of Electrical – Electronics, Faculty of Engineering and Natural Sciences, Kadir Has University, 34320 Istanbul, Turkey